

Journal of Materials Chemistry A

Accepted Manuscript



This is an *Accepted Manuscript*, which has been through the Royal Society of Chemistry peer review process and has been accepted for publication.

Accepted Manuscripts are published online shortly after acceptance, before technical editing, formatting and proof reading. Using this free service, authors can make their results available to the community, in citable form, before we publish the edited article. We will replace this *Accepted Manuscript* with the edited and formatted *Advance Article* as soon as it is available.

You can find more information about *Accepted Manuscripts* in the [Information for Authors](#).

Please note that technical editing may introduce minor changes to the text and/or graphics, which may alter content. The journal's standard [Terms & Conditions](#) and the [Ethical guidelines](#) still apply. In no event shall the Royal Society of Chemistry be held responsible for any errors or omissions in this *Accepted Manuscript* or any consequences arising from the use of any information it contains.

Porous $\text{LiNi}_{0.5}\text{Mn}_{1.5}\text{O}_4$ Sphere as 5V Cathode Material for Lithium Ion Batteries

Cite this: DOI: 10.1039/x0xx00000x

Jing Wang^a, Weiqing Lin^a, Bihe Wu^a, Jinbao Zhao^{*a,b}

Received 00th January 2012,
Accepted 00th January 2012

DOI: 10.1039/x0xx00000x

www.rsc.org/

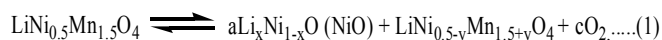
A new type of micro-sized porous spherical $\text{LiNi}_{0.5}\text{Mn}_{1.5}\text{O}_4$ (LNMO-Air) cathode material for lithium ion secondary battery has been synthesized by impregnation method using highly reactive nano-cupule MnO_2 spheres as manganese source. These LNMO-Air spheres are aggregates of nano-sized polyhedron particles with well-defined cubic spinel structure. They showed excellent rate capability and cycle stability, compared with other microspheres of LNMO. We also investigated the effect of trace amount of Mn^{3+} in the crystal structure on its specific capacity and cycle stability. Compared with the sample (LNMO- O_2) calcined in oxygen atmosphere, which is considered as Mn^{3+} free, LNMO-Air exhibits superior specific capacity, cycling ability and rate capability. Due to the existence of trace amount of Mn^{3+} , the LNMO-Air sample presents a discharge specific capacity of $108 \text{ mAh}\cdot\text{g}^{-1}$ at 5 C rate at 55 °C after 80 cycles without significant reduction. These improvements can be explained by better ion conductivity as the metal oxide layer spacing is enlarged to facilitate faster ion transfer and much improve electrical conductivity, both are attributed to the presence of Mn^{3+} .

Introduction

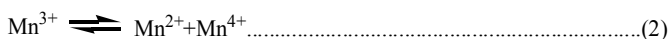
The upcoming new era of automobile-electric vehicle (EV), hybrid electric vehicle (HEV) and plug-in hybrid electric vehicle (PHEV), demands a rapid development of battery technology to meet their high energy density and high power density requirements.¹⁻³ Among all the types of batteries, lithium ion battery is one of the most likely candidates to fulfil the high energy demands, because of its many advantages such as high voltage, large specific capacity and excellent cycling performance.^{4,6} However, due to its intrinsic low ionic conductivity of organic electrolyte, compared with aqueous counterparts, its power capability is sluggish. In order to improve its power performance, many efforts have been made, among which is to reduce the particle size of electrode materials to the nanometer scale,⁷⁻¹³ Physically, the smaller the particles size is, the shorter the lithium ion diffusion distance and the electron transfer distance are, the better the rate capability is. The employment of nanomaterials in cell manufacture, on the other hand, has some disadvantages, such as high viscosity of slurry, low solid percentage, both of which lead to low active materials coated and thus low energy density. To achieve both excellent rate capability and high energy density, it is desired that the micrometer particles compose of aggregated nano-sized particles. In electrode processing, this kind of particles also leads to high loading and is able to better accommodate the volume change and to reduce the electrode tension upon cycling.¹⁴

Due to its low cost, low toxicity and good safety performance,¹⁵ spinel LiMn_2O_4 is considered to be an ideal cathode material for lithium-ion batteries. Moreover, by doping the spinel LiMn_2O_4 materials with a certain amount of transition metal elements M (M=Fe Co Ni Cr etc.), the Fermi

energies of the materials can be adjusted and their electrode potentials are raised as desired.^{16,17} Amongst the doped spinel cathode materials, $\text{LiNi}_{0.5}\text{Mn}_{1.5}\text{O}_4$ (LNMO) has been shown to have an acceptable performance and stable discharge capacity.¹⁶ This cathode shows a large charge/discharge platform at 4.7 V and a small platform around 4 V¹⁸. The platform around 4.7 V is assigned to the oxidation-reduction process of $\text{Ni}^{2+}/\text{Ni}^{4+}$ while the 4.0 V platform is attributed to the $\text{Mn}^{3+}/\text{Mn}^{4+}$ oxidation-reduction process. In real practice, the stoichiometry of LNMO is not perfect because when it is sintered above 600 °C to obtain good crystallinity, side reaction of generating oxygen voids and more Mn^{3+} cation is unavoidable:



However the effects of more Mn^{3+} in LNMO cathode are controversial. Some believe that the existence of Mn^{3+} is helpful to stabilize the cycling performance and to improve the stability.¹⁹ The Mn^{3+} induces more Ni and Mn disordering with a higher proportion of Fd3m lattice, thus improves Li ion transport coefficient and the electrical conductivity of LNMO. Others argue that Mn^{3+} ions have higher tendency to disproportionate²⁰:



Mn^{2+} ion can easily dissolve in electrolyte and is capable to electrochemically deposit at anode surface after passing through membrane,²¹ therefore it brings adverse influence for the cycling performance.

In our present work, we synthesized micro-sized spherical LNMO (LNMO-Air) comprised of aggregated nanopolyhedrons by an impregnation method and studied its electrochemical properties as cathode materials. In our two-step synthesis, we first prepared nanometer chestnut-cupule-like MnO_2 spheres and then impregnated it with an ethanol solution of LiNO_3 and $\text{Ni}(\text{NO}_3)_2 \cdot 6\text{H}_2\text{O}$, followed by solvents evaporation and high temperature calcination. The unique structured LNMO,^{20, 21} exhibits better rate capacity and cycle performance compared with the LNMO materials synthesized by using commercial MnO_2 as the original material in impregnation and ball-milling methods. We also prepared LNMO- O_2 in oxygen gas atmosphere with similar morphology but least oxygen voids to explore the influence of Mn^{3+} to its electrochemical performance.

Experimental section

Material preparation

The nanoscale chestnut-cupule-like MnO_2 spheres (MnO_2 -S) were prepared by a modified solvothermal method.²² An aqueous solution of 20 mmol MnSO_4 was mixed with 8 mL concentrated sulfuric acid, then $\text{K}_2\text{S}_2\text{O}_8$ solution was quickly poured into the solution under rapid stirring. The solution was kept in a water bath of 65 °C undisturbed for 18h. After filtration and washing with deionized water and ethanol, the product was dried in an oven at 100 °C. To synthesize LNMO-Air, 24 mmol of MnO_2 -S, 8 mmol of $\text{Ni}(\text{NO}_3)_2 \cdot 6\text{H}_2\text{O}$, and 17.28 mmol of LiNO_3 was dispersed into 20 ml ethanol. After grinded in a mortar for 30 minute, the solution was evaporated slowly at 80 °C under constant stirring. Finally, the obtained mixture was sintered in air at 800 °C for 20 h, then cooled down to room temperature slowly. The LNMO- O_2 sample was prepared in the exact same manner except that the final calcination was carried out in O_2 atmosphere. A similar procedure was employed to synthesize $\text{LiNi}_{0.5}\text{Mn}_{1.5}\text{O}_4$ (LNMO-C) using commercial available MnO_2 as manganese source. Commonly used ball milling method (FRITSCH-Pulverisette 14) was also tested to prepare $\text{LiNi}_{0.5}\text{Mn}_{1.5}\text{O}_4$ (LNMO-B), from a mixture of Li_2CO_3 , NiO and MnO_2 in the stoichiometric amount. The mixture of the solids was milled for 2h at 200r per minute and treated at 800 °C for 20 h in air.

Material characterization

The XRD patterns were collected on a Rigaku miniflex 600 instrument equipping with $\text{Cu K}\alpha$ radiation operated at 40kV and 15mA from 10° to 80° at 5° min^{-1} with a recording interval of 0.02°, while in XRD refinement, the scanning speed is 1° min^{-1} . Field emission scanning electron microscopy (SEM, HITACHI S-4800) was used to characterize the morphologies of samples, and energy dispersive X-ray spectroscopy (EDS, OXFORD 7426) was carried out to analyze the element composition on particle surface with 20kV acceleration voltage. Nitrogen adsorption and desorption data was collected on a Tristar 3000 system. The specific surface area analysis was, while the pore volume was performed by the BJH (Barrett-Joyner-Halenda) model. Fourier-transformed infrared spectra (FTIR) were determined with Nicolet 330 infrared spectrometer in transmittance mode (KBr pellet) over the range of 400-1000 cm^{-1} . Raman spectra (JOBIN Yvon Horiba Raman Spectrometer model HR800) were collected with 10 mW helium/neon laser at 632.8 nm excitation.

Electrochemical measurements

Electrochemical performances of these materials were evaluated in CR2016-type coin-cell configuration. The cathode electrode film was obtained by spreading a slurry (70 wt% active material, 20 wt% acetyleneblack and 10 wt% polyvinylidene difluoride (PVDF) binder were dispersed in N-methyl pyrrolidone (NMP) solvent) onto an aluminum foil using a doctor blade. After drying in a vacuum oven at 100 °C overnight, the electrode was punched out and roll-pressed. The coin cells were assembled by sandwiching a porous polyethylene separator between the electrode and Li metal foil in an Ar-filled glove box. The electrolyte used was 1 $\text{mol}\cdot\text{L}^{-1}$ LiPF_6 salt dissolved in a mixed solution of ethylene carbonate (EC) and dimethyl carbonate (DMC) with a weight ratio of 1:1 (#301 electrolyte, Guotai-Huarong New Chemical Materials Co., China).

The cells were galvanostatically charged and discharged on a battery test system (LAND CT-2001A instrument, Wuhan, China or NEWARE BTS type battery charger, Shenzhen, China) between 3.5-4.9V at room temperature. When the rates were higher than 1C (including 1C), in order to overcome the polarization of the battery at high rates, a two-step charge process (constant current and constant voltage charge) was employed.²³ Cyclic voltammogram (CV) measurements were performed on a CHI 660D potentiostat at a scan rate of 0.1 mV s^{-1} with voltage ranged from 3.4 to 5.0V. Electrochemical impedance spectra (EIS) were carried out on Solartron SI 1287 electrochemical workstation with frequency from 0.1 Hz to 100 kHz. All the tests were conducted at 25 °C except the high-temperature tests specified. The mass loading for all the cells was controlled in about 3 $\text{mg}\cdot\text{cm}^{-2}$.

Results and discussion

Fig.1 shows the SEM images of precursor compounds before impregnation reactions. Fig.1 (a) and (c) are the SEM images of synthesized MnO_2 -S spheres and commercial MnO_2 , respectively. The high-magnification SEM image of synthesized MnO_2 -S sphere is presented in Fig. 1(b). The micro-structures of these two materials are quite different. MnO_2 -S spheres are quite uniform in a size ranging from 2 μm to 4 μm . Each of these MnO_2 -S spheres is composed of many MnO_2 nano-needles radiating from its center, rendering the whole structure like a chestnut cupule. The nano-needles are well separated, generating a large space between adjacent nanorods, resulting in much larger surface area (shown below). The commercial MnO_2 particles are aggregation of small granules with low surface area. As shown in Fig. 1(d), commercial NiO particles are nanoparticles of 100s nm in diameter randomly stacked together.

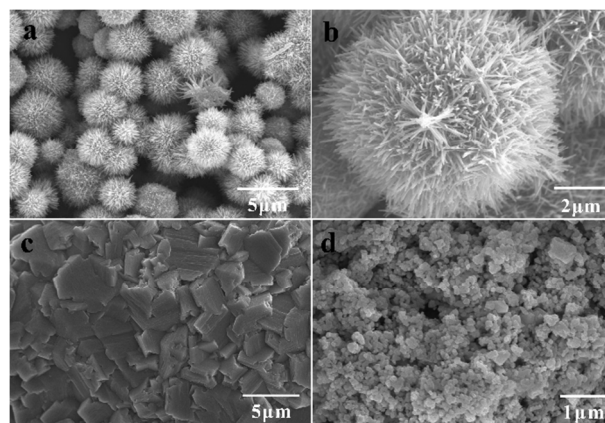


Fig.1 SEM images of the precursors (a) MnO_2 -S spheres, (b) magnified image of a single MnO_2 -S sphere, (c) commercial MnO_2 particles, (d) commercial NiO.

The N_2 adsorption/desorption analyse of chestnut-cupule-like MnO_2 -S spheres and the commercial MnO_2 are shown in Fig. 2. The BET total surface area and pore volume of the chestnut-like MnO_2 -S are $67 \text{ m}^2 \cdot \text{g}^{-1}$ and $0.116 \text{ cm}^3 \cdot \text{g}^{-1}$; much larger than that of the commercial MnO_2 , which are only $1.3 \text{ m}^2 \cdot \text{g}^{-1}$ and $0.002 \text{ cm}^3 \cdot \text{g}^{-1}$, respectively. The MnO_2 -S material exhibits an adsorption/desorption hysteresis, while the commercial MnO_2 material shows essentially a flat line. These features of MnO_2 -S larger surface area, bigger pore volume, and smaller nanostructures, make it a better candidate for impregnation process to form a more homogeneous material, therefore, the metal ions are more uniformly distributed in the structure.

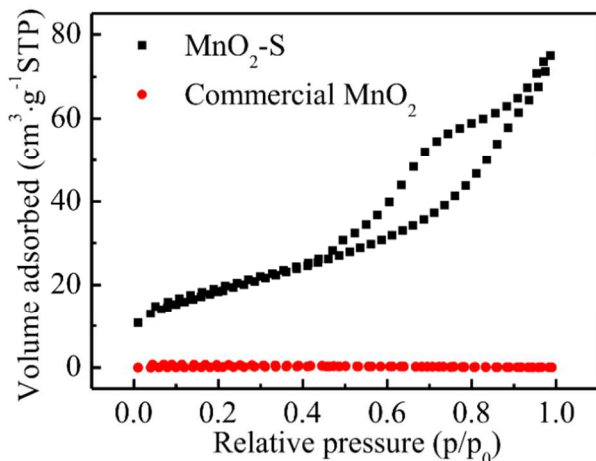


Fig. 2 Nitrogen adsorption-desorption isotherms of porous MnO_2 -S and commercial MnO_2 .

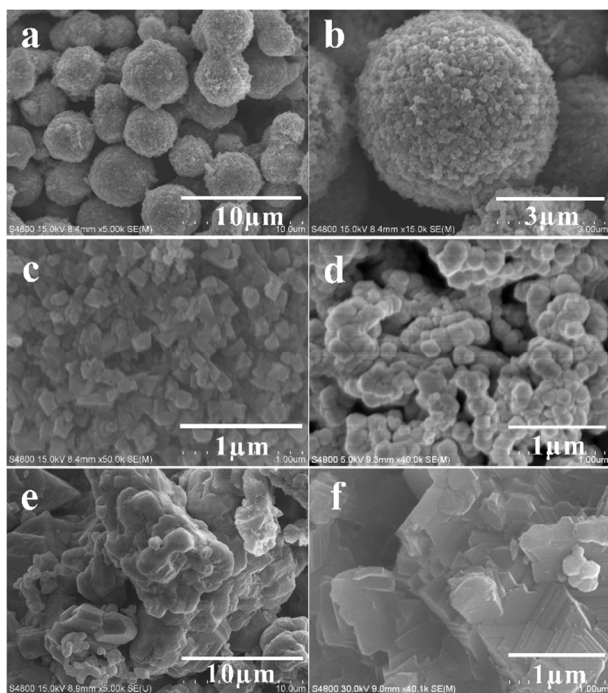


Fig.3 SEM images of (a) spherical LNMO-Air, (b) high magnified image of a single LNMO-Air, (c) high magnified image of a single LNMO-Air sphere surface, (d) LNMO-C, (e, f) LNMO-B.

The SEM images of morphologies and microstructures of the three synthesized LNMO materials are shown in Fig.3. The low-magnification SEM image (Fig. 3(a)) indicates that the LNMO-Air spheres are uniformly micron-sized spheres with diameters of 2–4 μm , which are similar to its MnO_2 -S precursor. Under high-magnification (Fig. 3(b-c)), it can be seen that these microspheres are made up of nano-polyhedrons with well-defined edges and planes, and these polyhedrons are fused together by vertex or/and plane. The LNMO-C (Fig. 3(d)), however, is constituted of diversely micron-sized particles with agglomeration to some extent. And more details are shown in Fig. S1. The LNMO-B (Fig. 3(e)) is large granular aggregate with some unreacted NiO nano-particles (Fig. S2) resulting in inhomogeneous distribution of metal ions. Results obtained from nitrogen adsorption and desorption curve are shown in Table S1 in supporting information. For the samples, LNMO-Air, LNMO-C and LNMO-B, their average surface area calculated using multipoint BET (Brunauer–Emmett–Teller) method are 4.6, 3.7 and $1.4 \text{ m}^2 \cdot \text{g}^{-1}$, the average pore radius obtained by use of BET model are 1.03, 0.26, 0.19 nm and the average pore volume observed by the BJH method are 0.025, 0.0082 and $0.0024 \text{ cm}^3 \cdot \text{g}^{-1}$, respectively. It can be found that LNMO-Air is bigger than the other samples in the average surface area, pore radius and average pore volume, which is consistent with their structure of the precursors and SEM results.

The TEM characterization of the LNMO-Air is displayed in Fig. 4. As shown in Fig. 4(a), the LNMO-Air is of hollow structures, which is consistent with the BET results. SAED pattern (Fig. 4(a) inset) of the whole micron-sized LNMO-Air sphere at bottom of Fig. 4(a) shows unordered diffraction spots, implying the polycrystalline structure of entire LNMO-Air sphere. After fully grinding, a single nano-sized polyhedron as shown in Fig. 4(b) is obtained from the micron-sized LNMO-Air sphere. SAED pattern (Fig. 4(c)) with the electron beam in the [110] direction corresponding to Fig. 4(b) presents well-organized array of diffraction spots that index a typical spinel lattice structure. This means the polycrystalline LNMO-Air micron-sized sphere is composed of monocrystalline nano-sized polyhedrons. A high-resolution TEM (HRTEM) image of the nano-sized polyhedron of Fig. 4(b) appears clear lattice fringes (Fig. 4(d)). The interplanar spacing lattice is 0.48nm, which is

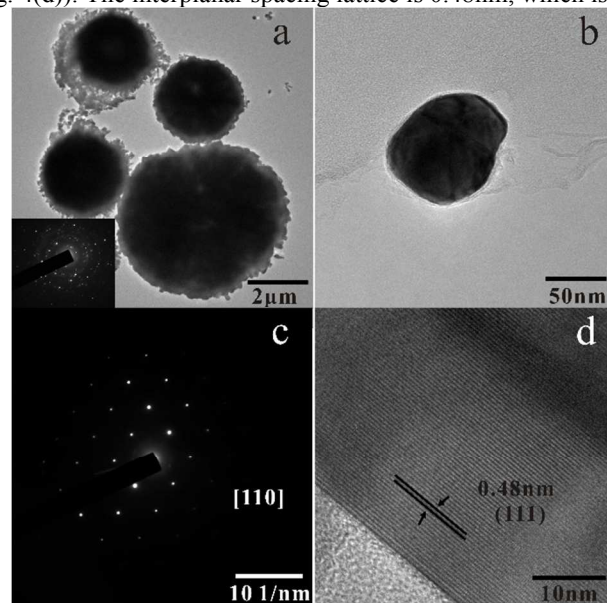


Fig.4. TEM images of (a) the as-prepared LNMO-Air and (b) a nano-sized polyhedron obtained from LNMO-Air sphere by fully grinding. (c)

SAED pattern in the [110] zone of nano-sized polyhedron corresponding to (b); (d) HRTEM image of the nano-sized polyhedron

in accordance with the d-spacing of the (111) crystal planes of the $\text{LiNi}_{0.5}\text{Mn}_{1.5}\text{O}_4$. The ordered lattices in long-range order result in the intercalation and deintercalation of Li ion easily occurring, which is favourable for the rate property.

The LNMO structures are further proved by XRD patterns, as shown in Fig. 5. In Fig. 5, the XRD patterns of three samples are plotted. From these patterns, all three can be indexed to cubic spinel structure (JCPDS Card No.: 80-2162) with impurity (peaks of $2\theta = 37.335^\circ$, 43.381° and 63.024° ²⁴) which is indexed as rock salt phase ($\text{Li}_x\text{Ni}_{1-x}\text{O}/\text{NiO}$). However, the relative diffraction intensities of rock salt phase in LNMO-C and LNMO-B are much stronger than that of LNMO-Air. The present of less rock salt phase impurity in LNMO-Air is attributed to the more porous structure and smaller particle size of $\text{MnO}_2\text{-S}$ precursor. The more open structure renders better impregnation, the smaller particle size facilitates kinetically more homogeneous ion ordering.

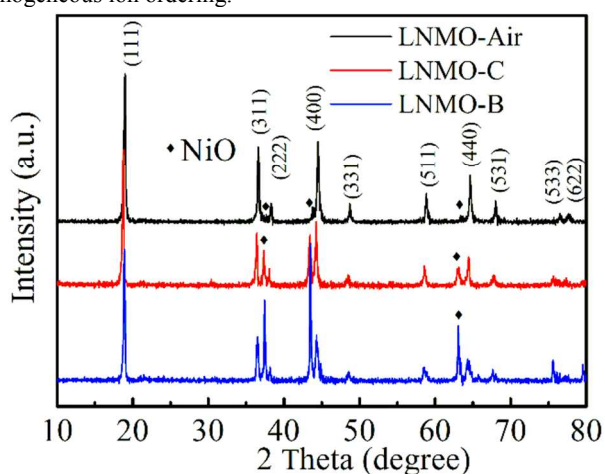
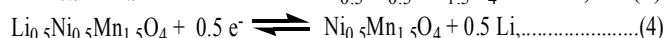


Fig. 5 XRD patterns of spherical LNMO-Air, LNMO-C and LNMO-B.

Fig. 6 presents the charge–discharge profiles of the samples at the rate of 0.5C ($74\text{mA}\cdot\text{g}^{-1}$) between 3.5 and 4.9 V at 25 °C. All three samples show very slow specific discharge capacity decay (Fig. 5 (a)), and their specific discharge capacities are quite different. For example, in the fifth cycle, the LNMO-Air shows the highest specific discharge capacity at $118\text{mAh}\cdot\text{g}^{-1}$, while LNMO-C and LNMO-B cathode materials only deliver specific capacity of $76\text{mAh}\cdot\text{g}^{-1}$ and $87\text{mAh}\cdot\text{g}^{-1}$, respectively. Beside the smaller particle size and the better morphology of LNMO-Air, the better ion ordering in LNMO-Air is believed to have more profound effect on its higher specific discharge capacity. The columbic efficiencies for sample test were shown as Fig. S3 in supporting information. The columbic efficiencies of the initial few cycles is low, especially for the first cycle, which is attributed to the decomposition of #301 electrolyte and catalysis action of Ni and Mn ion in the spinel material. After 10 cycles, its columbic efficiencies are maintained at 98.2%. The decomposition of electrolyte actually occurred, but was maintained at an acceptable level after several cycles, which guarantees our cell a long life. Generally, the irreversible capacity loss in the first cycle corresponds to the formation of a solid surface layer by the oxidation of the electrolyte.²⁵ The irreversible capacity loss on each cycle is attributable to the oxidation of the electrolyte and the formation of an unstable solid surface film in the following cycles.²⁵ Cyclic voltammograms experiment of commercial electrolyte was carried out by use of the coin cell

with a blank cathode and lithium film as anode on a CHI 660D potentiostat at a scan rate of $0.1\text{mV}\cdot\text{s}^{-1}$ during a voltage range from 3.4 to 5.0V (Fig. S4 in supporting information). After the first cycle, the oxidation currents become lower, so the decomposition of electrolyte is relieved. The discharge capacity–voltage profile in Fig. 6 (b) can shed light on the origin of the difference. All three materials show two flat voltage plateaus, one is around 4.7V and the other is around 4 V, but the magnitudes are drastically different. LNMO-Air has the largest 4.7V plateau, but the smallest 4.0V plateau, while LNMO-B has the smallest 4.7V one, largest 4.0V one. The 4.7V plateau corresponds to the reaction:



The plateau around 4.0 V, however, is from the side reaction of $\text{Mn}^{4+}/\text{Mn}^{3+}$. The more homogeneous metal ion ordering results in larger 4.7 V plateau, the more the non-uniform distribution of Ni and Mn, the larger the 4 V is, even though the instability of LNMO at high-temperature calcination makes a small contribution to it. Thus it is clear that LNMO-Air has the best metal ion ordering among these samples, which indicates that $\text{MnO}_2\text{-S}$ is a much better precursor for LNMO material. Cyclic voltammogram curves of these samples are shown in Fig. S5. The LNMO-Air exhibits two major redox peaks in the region of 4.7–4.9 V and a very small peak at around 4.0 V, while for LNMO-C and LNMO-B, two major redox range 3.8–4.4V and 4.5–4.9V emerge, which are accordance with the discharge curve (Fig. 6(b)).

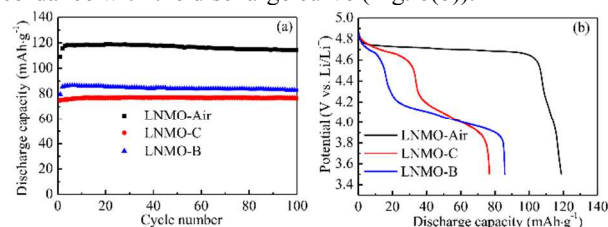


Fig. 6 Electrochemical properties of the as prepared samples at 25 °C. (a) cycle performance at 0.5C; (b) the 20th discharge curve at 0.5C;

Fig. 7 shows the comparison of electrochemical performance of these LNMO at different rates. All three samples show their specific capacities at 1.0 C is slightly higher than that at 0.5 C, which is also reported by Zhou²³ and Lazarraga²⁵ without clear conclusion. This possibly caused by different charging process between 0.5C and 1C. In our experiment, the cells were galvanostatically charged and discharged on a battery test system between 3.5–4.9V at room temperature at low rates. When the rates higher than 1C (including 1C), a two-step charge process (constant current and constant voltage charge) was employed in order to overcome the polarization of the battery at high rates. In the latter case, following the constant current charge step, the constant voltage charge process was carried out till the current reduced to one tenth of its initial constant value. Among these samples, the LNMO-Air does not only exhibit the much higher capacity than the other two (about 50% more), but also a better rate capability. At a low rate of 0.2 C ($29\text{mA}\cdot\text{g}^{-1}$), LNMO-Air delivers a discharge capacity of $123\text{mAh}\cdot\text{g}^{-1}$, which is 83.6% of the theoretical capacity of LNMO ($147\text{mAh}\cdot\text{g}^{-1}$). It delivers 86% and 82% of 0.2 C discharge capacity at 5 C ($735\text{mA}\cdot\text{g}^{-1}$), and at 10 C ($1470\text{mA}\cdot\text{g}^{-1}$), respectively, which are all considerably higher than that of commonly reported sub-micron LNMO, or nano-LNMO. On the other hand, LNMO-C and LNMO-B can only deliver a

discharge capacity of $82 \text{ mAh}\cdot\text{g}^{-1}$ and $86 \text{ mAh}\cdot\text{g}^{-1}$ at 0.2 C, respectively. At 5C rates, they show specific discharge capacity of $73 \text{ mAh}\cdot\text{g}^{-1}$ and $71 \text{ mAh}\cdot\text{g}^{-1}$, with comparable retention percentage to LNMO-Air. Once the current is raised to 10 C, the discharge capacity of LNMO-C and LNMO-B is only $59 \text{ mAh}\cdot\text{g}^{-1}$ (72%) and $57 \text{ mAh}\cdot\text{g}^{-1}$ (66%) respectively, both are much lower retention percentage than LNMO-Air. After 50 cycles with successive charge-discharge rate variation, all the materials can recover to their original specific discharge capacities when charge/discharge rate returns to 0.2 C. The excellent rate capability of the LNMO-Air is due to its unique porous structure.¹⁴ In this particular structure, both micropores between the micro-size particles and nanopores between the nanoparticles are present, generating high active surface area for better wetting the electrode by electrolyte and shortening Li^+ ions diffusion distance, thus a better rate capability is attained.

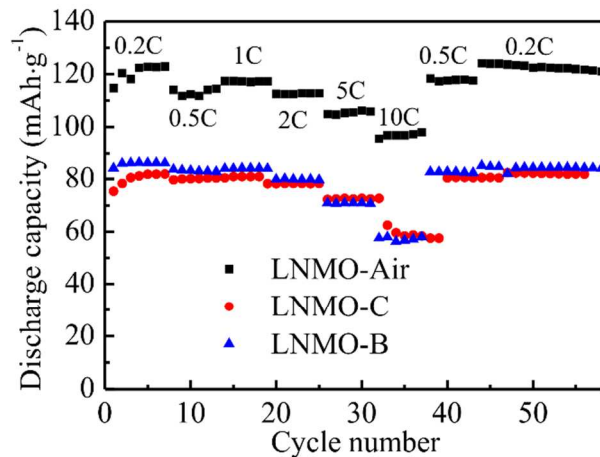


Fig. 7 Rate cycling performance of samples.

The role of Mn^{3+} in LNMO materials is controversial, and still under debating. Hagh²⁶ have proposed that the existence of Mn^{3+} is adverse for the reversible Li ion extraction/insertion reaction especially at a higher cycle rate and high temperature. By the attack of trace amount of HF, Mn^{3+} ions are known to undergo a disproportionation reaction²⁰ to form Mn^{2+} and Mn^{4+} ions. Mn^{2+} ions are readily dissolved into electrolyte and can be reduced to Mn metal on the anode surface,²¹ the resulting Mn film prevents Li ion transportation, causing significantly capacity decline during the cycling. However, Zhang¹⁸ argued that the existence of Mn^{3+} promoted more disordered amongst the metal sites that facilitated the Li^+ transport, especially for the high rate. In order to further explore the influence of Mn^{3+} , we synthesized LNMO materials without Mn^{3+} ions present, by calcining the impregnated $\text{MnO}_2\text{-S}$ particles in O_2 atmosphere.²⁷ This Mn^{3+} ion free LNMO material is denoted as LNMO- O_2 .

In order to capture the fine-structure difference, XRD refinements on LNMO-Air and LNMO- O_2 with slow scan speed of $1^\circ\cdot\text{min}^{-1}$ were conducted and the data are shown in Fig. 8. As expected, both samples show strong spinel structure peaks at $2\theta = 18.75^\circ$, 36.40° , 44.32° and 64.44° , and the peak intensity ratio of NiO at 63.42° and LNMO at 18.95° for LNMO-Air is bigger than that of LNMO- O_2 , suggesting that the NiO content in LNMO-Air is bigger than that in LNMO- O_2 . It is understood that the electrochemical properties are not necessarily decided by the optimized crystallographic structure, they indeed require appropriate concentration of oxygen vacancies and Fd3m configuration.²⁸ The lattice parameters, d_{111} and size of sub-grain calculate by Scherrer Equation along (111) surface are obtained from the least square

refinement based on a cubic structure using PDXL2 software (Rigaku, Japan), and the results are summarized in Table 1. The crystal lattice parameter and interlayer space of (111) lattice plane for the LNMO-Air are 8.1740 \AA and 4.7266 \AA , and for LNMO- O_2 are 8.1656 \AA and 4.7175 \AA , both are shorter in LNMO- O_2 . This is because that calcination in air atmosphere leads to more oxygen vacancies than in O_2 atmosphere. To keep charge neutrality, more Mn^{3+} was thus generated in LNMO-Air. The ionic radius of Mn^{3+} (0.645 \AA) is larger than Mn^{4+} (0.530 \AA). As a result, the crystal lattice parameter and interlayer space of (111) lattice plane for the LNMO-Air are a slight larger than that of LNMO- O_2 .

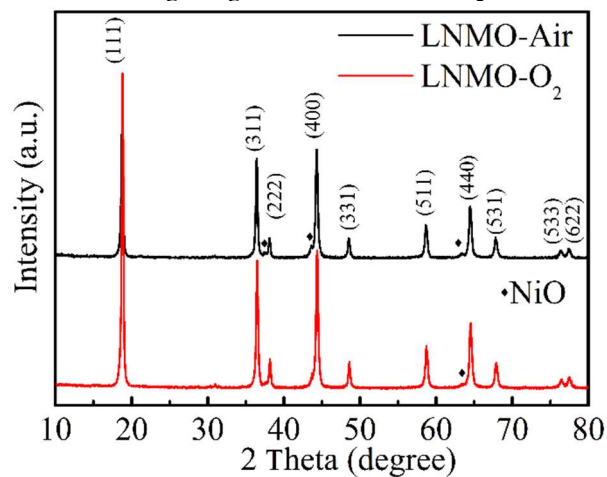


Fig. 8 XRD patterns of samples.

Table 1 The summary of the as-synthesized samples of lattice parameters for all samples (a, b, c, a=b=c), d_{111} , size of sub-grain calculated by Scherrer Equation along (111) surface and the integrated intensity ratios of the (400)/(311).

	Lattice parameter (\AA)	$d_{(111)}$ (\AA)	Sub-grain size (\AA)
LNMO- O_2	8.1656	4.7175	359.22
LNMO-Air	8.1740	4.7266	365.36

There are not any visible differences in the LNMO- O_2 and LNMO-Air by SEM characterization (Fig. S7). IR spectroscopy is an effective technique in identifying the subtle difference between $\text{P4}_3\text{32}$ and $\text{Fd}3\text{m}$ spinels of LNMO.²⁹ The IR spectra of these samples are shown in Fig. 9. The vibration bands at 650 and 428 cm^{-1} , which are present in LNMO- O_2 but absent in LNMO-Air, are indicative of a $\text{P4}_3\text{32}$ crystallographic structure,⁶ on the other hand, the $\text{Fd}3\text{m}$ crystal lattice exhibits peak at 587 cm^{-1} . The characteristic of $\text{Fd}3\text{m}$ crystallographic structure lies in the fact that the band intensity of 622 cm^{-1} is higher than that of 587 cm^{-1} ,³⁰ which is clear seen in LNMO-Air spectrum. Thus we can conclude that LNMO- O_2 calcined in O_2 atmosphere exhibit cation ordered $\text{P4}_3\text{32}$ phase, and LNMO-Air calcined in air presents cation ordered $\text{Fd}3\text{m}$ spinel.

The difference between LNMO-Air and LNMO- O_2 can also be examined by Raman spectroscopy, as shown in Fig. 10. According to previous reports,^{31, 32} the strong band appeared at 649 cm^{-1} is attributed to the symmetrical Mn-O stretching vibration (A_{1g}) in

MnO₆ octahedra. Peaks around 416 and 510 are related to the Ni²⁺-O stretching mode in spinel. T_{2g}⁽³⁾ band of the spinel is at around 600-625 cm⁻¹. The split of this T_{2g}⁽³⁾ band is the fingerprint of P4₃32 space group. The splitting of T_{2g}⁽³⁾ can be clearly seen for LNMO-O₂, as a doublet at 621 and 604 cm⁻¹ is observed. The other characteristic peaks of P4₃32 structure are around 249, 228 and 170 cm⁻¹, which are all present in LNMO-O₂ spectrum.^{6, 32, 33} In LNMO-Air Raman spectrum, all these features referring to Fd3m structure are absent. Thus, we are confident that LNMO-O₂ is P4₃32 spinel.

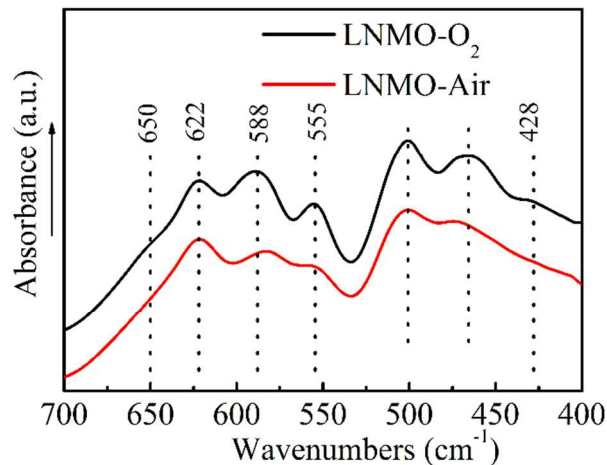


Fig. 9 FT-IR spectra of LNMO-Air and LNMO-O₂ samples.

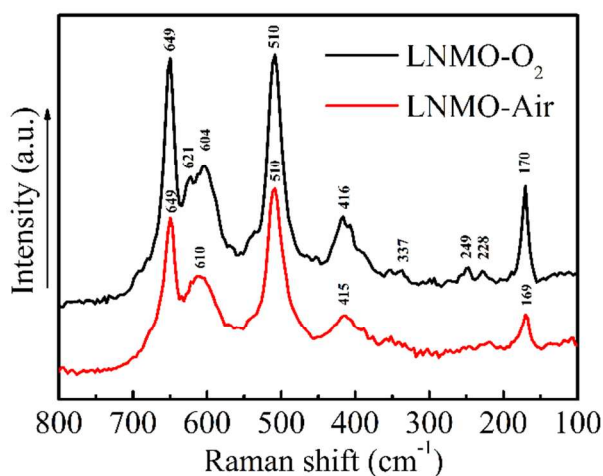


Fig. 10 Raman spectra of LNMO-Air and LNMO-O₂ samples.

Fig. 11 shows the cyclic voltammograms of the LNMO-O₂ and LNMO-Air in button cells. The two curves are similar with two redox peaks in the region of 4.7-4.9 V, and a very small peak around 4.0 V. The two redox peaks in the region of 4.7-4.9 V are assigned to the Ni²⁺/Ni³⁺ and Ni³⁺/Ni⁴⁺ redox couples at 4.7 V and 4.75 V. However, the tiny current peak near 4.0 V, corresponding to the Mn³⁺/Mn⁴⁺ redox couple, for LNMO-Air can not be neglected, while for LNMO-O₂ it is too small to have significant effect on its discharge capacity. This is accordance with XRD refinement, IR spectra and Raman results that there is a small amount of Mn³⁺ in LNMO-Air, while it is almost no present in LNMO-O₂.

Typical discharge curves and cycle performances of the two samples at room temperature are shown in Fig. 12. Both the LNMO-Air and LNMO-O₂ have a dominant plateau around 4.7 V (Fig 12. (a)), the difference is that there is a small plateau at about 4.0 V for LNMO-Air (Fig. 12(a) inset), while for LNMO-O₂, this plateau is

unobservable. The discharge cycling performance of these materials at 1 C are shown in Fig. 12 (b). The first discharge capacities of LNMO-Air and LNMO-O₂ are comparable, 122 and 120.5 mAh·g⁻¹, respectively. Their discharge capacity retentions are also comparable, 94.6% and 94.1% after 200 cycles, respectively. The rate capabilities of these two materials have apparent differences, as shown in Fig. 12(c): at low rate (0.2 C-1 C), LNMO-O₂ exhibits slightly higher discharge capacity than LNMO-Air; at an intermediate rate (2 C) their specific capacities are the same; at high rates (5 C-10 C), however, the specific capacity of LNMO-Air becomes larger than that of LNMO-O₂. We believe that the existence of Mn³⁺ ions causes this difference. In Fd3m lattice,¹⁹ the existence of Mn³⁺ ions generates more disordering among the Ni sites and Mn sites, which is beneficial to Li ion transportation³⁴ as well to electron conductivity. There are two additional electron hopping pathways which are absent in P4₃32: Ni^{2+/3+} → Mn⁴⁺ → Ni^{3+/4+} and Ni^{2+/3+} → Mn⁴⁺ ↔ Mn³⁺ → Ni^{3+/4+}.²⁹ With these additional electron hopping pathways, charges can be transferred faster, which helps to relieve the ohmic polarization and electrochemical polarization in the materials,³⁵ and thus a better cycling LNMO material especially at higher rates.

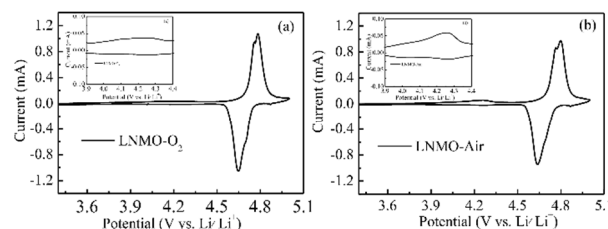


Fig. 11 Cyclic voltammogram curves (0.1 m V s⁻¹) of (a) spherical LNMO-O₂ sample, (b) spherical LNMO-Air sample.

In order to verify our assumption, EIS was measured in the range from 100 kHz to 0.1 Hz after 30 cycles at 1 C rate, as shown in Fig. 12(d). The Nyquist plots of both materials display the similar profile, displaying a semicircle in the high-frequency region and a linear slope in the low-frequency region. Both the equivalent circuits are the same as insets shown Fig. 12 (d). The R_s is assigned to electrolyte resistance, while the R_{ct} is attributed to direct charge transfer resistance of electrode materials. The EIS results clearly shows that the charge transfer resistance of the LNMO-Air (21.2 Ω) is much smaller than that of the LNMO-O₂ (52.2 Ω), which agrees well with our hypothesis that the small amount of Mn³⁺ in LNMO-Air generated by calcination in air atmosphere, lowers the barriers for Li⁺ ion transportation and electron conducting thus improve its rate capacity at high rates.

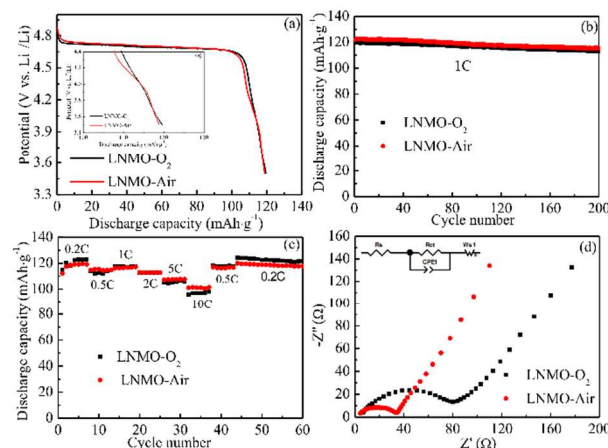


Fig.12 Electrochemical properties of the as prepared samples at 25 °C (a) cycle performance at 1C; (b) the 20th discharge curve at 1C; (c) rate cycling performance. (d) EIS spectra of the LNMO-O₂ and LNMO-Air in the frequency range between 0.1 Hz and 100 kHz.

The present of Mn³⁺ ions in LNMO-Air also greatly improves its electrochemical performance at high temperature (55 °C), as shown in Fig. 13. The discharge capacity (Fig. 13 (a)) of LNMO-Air does not deteriorate, however, the cycle life of LNMO-O₂ shows a sudden death after 30 cycles, meaning the latter is not an electrode material suitable for high temperature application. By examining their relationships between discharge capacity and voltage, we can see the obvious differences: the LNMO-Air material is able to retain its 4.7 V plateau throughout 40 cycles, but the LNMO-O₂ material drops its plateau from 4.58 V to 4.12 V as cycled, and the magnitude of the plateau is also constantly shrinking. This dramatic different behaviour likely results from that the LNMO-O₂ cathode is higher polarized than the LNMO-Air cathode due to their quite different ion and electronic conductivities, as discussed above. EIS studies unambiguously demonstrate their R_{ct} different behaviours Fig. 13 (c, d). It can be seen that the R_{ct} of all samples at 55 °C is higher than that at 25 °C. According to Seung M. Oh's research,³⁶ the surface film became enrichment by inorganic fluorinated species and turned thicker with cycling at elevated temperature, resulting in a continued electrode polarization and even cell invalidation. This similar phenomenon was also reported by Markovsky's study.³⁷ LiF, C-F and P-F_x species were formed at the surface of aged LiNi_{0.5}Mn_{1.5}O₄ electrode operating at high temperature.³⁷ These oxidative products acted as an electrically insulating layer that could decrease the electronic conductivity and impede the transportation of ions.²⁸ The R_{ct} of LNMO-O₂ cathode increases from 172 Ω to 469 Ω, while that of LNMO-Air only changes from 79 Ω to 103 Ω. As the resistance of LNMO-O₂ electrode keeps increasing as the cycling goes on, its performance gets worse and worse; on the other hand, with Mn³⁺ ions present in LNMO-Air, its ion and electron conductivities are much improved, its electrode polarization is greatly reduced, and its performance is perfectly preserved. The electrical performance and capacity retention of LNMO-Air sphere are comparable to other reported LNMO.^{38,39} The electrical performance at high rate⁴⁰ and elevated temperature⁴¹ are even better.

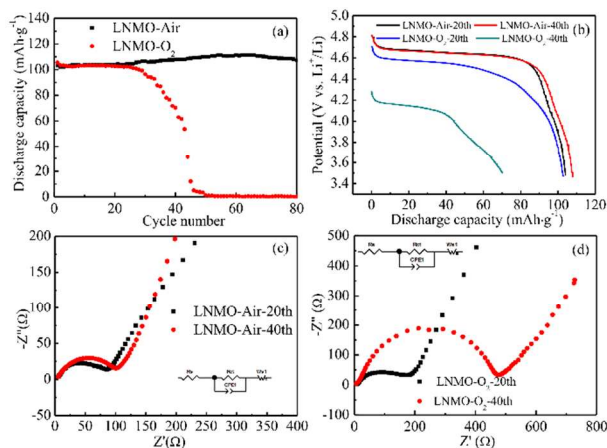


Fig.13 Electrochemical properties of the LNMO-O₂ and LNMO-Air as prepared samples at 55 °C (a) cycle performance at 5C (735 mA·g⁻¹); (b) the 20th and 40th discharge curve at 5C; (c, d) EIS spectra in the frequency range between 0.1 Hz and 100 kHz.

Conclusions

In summary, the porous micron-sized sphere LiNi_{0.5}Mn_{1.5}O₄ particles were synthesized via an impregnation method based on highly prominent nano-thorn MnO₂ spheres as the manganese sources. The obtained materials were of good crystalline with a particle size of approximately 2-4 μm composed of nano-size polyhedron. In comparison to conventionally ball-milling method, the method presented here can be easily operated and is energy-efficient. The electrochemical properties of the sphere LiNi_{0.5}Mn_{1.5}O₄ cathode material was superior to those made from commercial manganese sources and conventional approaches, because of its more porous structure for the enhanced immersion of electrolyte and better structure for insertion/desertion of Li ions. We also studied the effects of the trace amount of Mn³⁺ ions in the structure on its specific capacity and cycle stability. We proposed that these trace Mn³⁺ ions are beneficial to its rate capability and cycle life, especially at high rates and raised temperature, by improving the conductivities of Li ions and electrons of the LNMO material.

Acknowledgments

The authors gratefully acknowledge the financial supports from the National High Technology Research and Development Program of China (2012AA110204) and Key Project of Science and Technology of Fujian Province (2013H6022). Weiqing Lin expresses his special thanks to National Found for Fostering Talents of Basic Science (J1310024). The authors also wish to express their thanks to Drs. Dong Sun, Peng Zhang, and Jing Yang for their valuable suggestions.

Notes and references

^a State Key Lab of Physical Chemistry of Solid Surfaces, Department of Chemistry, Collaborative Innovation Center of Chemistry for Energy Materials, College of Chemistry and Chemical Engineering, Xiamen University, Xiamen, 361005, P. R. China.

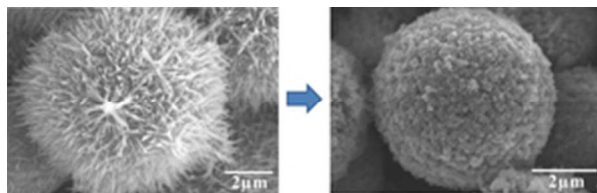
^b School of Energy Research, Xiamen University, Xiamen, 361005, P.R. China.

E-mail: jbzhaoy@xmu.edu.cn

† Electronic Supplementary Information (ESI) available: EDS element mapping of LNMO-C and LNMO-B; SEM of LNMO-O₂ and LNMO-Air. See DOI: 10.1039/b000000x/

- D. Liu, J. Trottier, P. Charest, J. Fréchet, A. Guerfi, A. Mauger, C. M. Julien and K. Zaghib, *J. Power Sources*, 2012, **204**, 127-132.
- S. Yang, J. Chen, Y. Liu and B. Yi, *J. Mater. Chem. A*, 2014.
- J. Yang, F. Cheng, X. Zhang, H. Gao, Z. Tao and J. Chen, *J. Mater. Chem. A*, 2014, **2**, 1636-1640.
- Z. Yang, J. Zhang, M. C. W. Kintner-Meyer, X. Lu, D. Choi, J. P. Lemmon and J. Liu, *Chem. Rev.*, 2011, **111**, 3577-3613.
- X. Li, H. Lin, W. Cui, Q. Xiao and J. Zhao, *ACS Appl. Mater. Interfaces*, 2014.
- G. B. Zhong, Y. Y. Wang, X. J. Zhao, Q. S. Wang, Y. Yu and C. H. Chen, *J. Power Sources*, 2012, **216**, 368-375.
- J. Lu, Q. Peng, W. Wang, C. Nan, L. Li and Y. Li, *J. Am. Chem. Soc.*, 2013.
- F. Fu, G. L. Xu, Q. Wang, Y. P. Deng, X. Li, J. T. Li, L. Huang and S. G. Sun, *J. Mater. Chem. A*, 2013.
- W. Tang, Y. Hou, F. Wang, L. Liu, Y. Wu and K. Zhu, *Nano Lett.*, 2013, **13**, 2036-2040.
- E. Hosono, T. Kudo, I. Honma, H. Matsuda and H. Zhou, *Nano Lett.*, 2009, **9**, 1045-1051.
- Y. Wu, Z. Wen, H. Feng and J. Li, *Small*, 2012, **8**, 858-862.
- W. J. Cui, H. J. Liu, C. X. Wang and Y. Y. Xia, *Electrochem. Commun.*, 2008, **10**, 1587-1589.

13. H. Zhou, S. Zhu, M. Hibino, I. Honma and M. Ichihara, *Adv. Mater.*, 2003, **15**, 2107-2111.
14. S. Liang, J. Yi and A. Pan, *Int. J. Electrochem. Sci.*, 2013, **8**, 6535-6543.
15. Y.L. Ding, J. Xie, G.S. Cao, T.J. Zhu, H.M. Yu and X.B. Zhao, *Adv. Funct. Mater.*, 2011, **21**, 348-355.
16. Y. Wang, G. Yang, Z. Yang, L. Zhang, M. Fu, H. Long, Z. Li, Y. Huang and P. Lu, *Electrochim. Acta*, 2013, **102**, 416-422.
17. G. Q. Liu, L. Wen and Y. M. Liu, *J. Solid State Electrochem.*, 2010, **14**, 2191-2202.
18. J. Xiao, X. Chen, P. V. Sushko, M. L. Sushko, L. Kovarik, J. Feng, Z. Deng, J. Zheng, G. L. Graff, Z. Nie, D. Choi, J. Liu, J.G. Zhang and M. S. Whittingham, *Adv. Mater.*, 2012, **24**, 2109-2116.
19. B. Hai, A. K. Shukla, H. Duncan and G. Chen, *J. Mater. Chem. A*, 2013, **1**, 759-769.
20. S. Brutti, G. Greco, P. Reale and S. Panero, *Electrochim. Acta*, 2013, **106**, 483-493.
21. J.H. Kim, N. P. W. Pieczonka, Z. Li, Y. Wu, S. Harris and B. R. Powell, *Electrochim. Acta*, 2013, **90**, 556-562.
22. H.E. Wang and D. Qian, *Mater. Chem. Phys.*, 2008, **109**, 399-403.
23. L. Zhou, D. Zhao and X. Lou, *Angew. Chem.*, 2012, **124**, 243-245.
24. J. Song, D. W. Shin, Y. Lu, C. D. Amos, A. Manthiram and J. B. Goodenough, *Chem. Mat.*, 2012, **24**, 3101-3109.
25. J. B. Goodenough and Y. Kim, *Chem. Mat.*, 2009, **22**, 587-603.
26. L.W. Ma, B.Z. Chen, X.C. Shi, W. Zhang and K. Zhang, *Colloids Surf. A*, 2010, **369**, 88-94.
27. J. H. Kim, S. T. Myung, C. S. Yoon, S. G. Kang and Y. K. Sun, *Chem. Mat.*, 2004, **16**, 906-914.
28. C. M. Julien and A. Mauger, *Ionics*, 2013, **19**, 951-988.
29. Y.C. Jin, C.Y. Lin and J.G. Duh, *Electrochim. Acta*, 2012, **69**, 45-50.
30. Z. Zhu, Qilu, D. Zhang and H. Yu, *Electrochim. Acta*, 2014, **115**, 290-296.
31. C. M. Julien and M. Massot, *Mater. Sci. Eng. B*, 2003, **97**, 217-230.
32. S. H. Oh, K. Y. Chung, S. H. Jeon, C. S. Kim, W. I. Cho and B. W. Cho, *J. Alloy Compd.*, 2009, **469**, 244-250.
33. G. B. Zhong, Y. Y. Wang, Y. Q. Yu and C. H. Chen, *J. Power Sources*, 2012, **205**, 385-393.
34. J. Cabana, M. Casas-Cabanas, F. O. Omenya, N. A. Chernova, D. Zeng, M. S. Whittingham and C. P. Grey, *Chem. Mat.*, 2012, **24**, 2952-2964.
35. O. Sha, Z. Tang, S. Wang, W. Yuan, Z. Qiao, Q. Xu and L. Ma, *Electrochim. Acta*, 2012, **77**, 250-255.
36. J. Mun, T. Yim, K. Park, J. H. Ryu, Y. G. Kim and S. M. Oh, *J. Electrochem. Soc.*, 2011, **158**, A453-A457.
37. D. Aurbach, B. Markovsky, Y. Talyossef, G. Salitra, H.J. Kim and S. Choi, *J. Power Sources*, 2006, **162**, 780-789.
38. T. Yang, K. Sun, Z. Lei, N. Zhang and Y. Lang, *J. Alloy Compd.*, 2010, **502**, 215-219.
39. J. C. Arrebola, A. Caballero, L. Hernán and J. Morales, *J. Power Sources*, 2008, **180**, 852-858.
40. D. Liu, J. Han and J. B. Goodenough, *J. Power Sources*, 2010, **195**, 2918-2923.
41. Y. Fan, J. Wang, Z. Tang, W. He and J. Zhang, *Electrochim. Acta*, 2007, **52**, 3870-3875.



A new type of micro-sized porous spherical $\text{LiNi}_0.5\text{Mn}_1.5\text{O}_4$ (LNMO-Air) cathode material for lithium ion secondary battery has been synthesized by impregnation method using highly reactive nano-cupule MnO_2 spheres as manganese source. These LNMO-Air spheres are aggregates of nano-sized polyhedron particles with well-defined cubic spinel structure. They showed excellent rate capability and cycle stability, compared with other microspheres of LNMO. We also investigated the effect of trace amount of Mn^{3+} in the crystal structure on its specific capacity and cycle stability. Compared with the sample (LNMO-O2) calcined in oxygen atmosphere, which is considered as Mn^{3+} free, LNMO-Air exhibits superior specific capacity, cycling ability and rate capability. Due to the existence of trace amount of Mn^{3+} , the LNMO-Air sample presents a discharge specific capacity of $108 \text{ mAh}\cdot\text{g}^{-1}$ at 5 C rate at 55 °C after 80 cycles without significant reduction.

These improvements can be explained by better ion conductivity as the metal oxide layer spacing is enlarged to facilitate faster ion transfer and much improve electrical conductivity, both are attributed to the presence of Mn^{3+} .

25x7mm (300 x 300 DPI)